Finite Element Analysis Of 2-D Tubular Braided Composite Based on Geometrical Models to Study Mechanical Performances

Authors: Ali Gholami[1], Garrett W. Melenka[1]*

[1]*Department of Mechanical Engineering, York University, Toronto, Canada*

*Corresponding Author: gmelenka@yorku.ca

Finite Element Analysis Of 2-D Tubular Braided Composite Based on Geometrical Models to Study Mechanical Performances

Tubular Braided Composites (TBC) have a higher strength to weight ratio than conventional materials and better mechanical properties compared to laminated composite materials. The optimization of the TBC and the introduction of new applications requires a comprehensive understanding of TBC's behaviour. One efficient way to study the behaviour of TBC is using Finite Element Modelling (FEM). This paper will introduce a method for generating geometrical models with different patterns and variables. Micro Computed-Tomography (μCT) is also used for generating an actual 3-D model of a TBC. The geometrical model and the μCT models are visually compared. The geometrical model is inputted into the FEM software package and is studied in different conditions. Finally, the result of FEM is compared against experimental and analytical results.

Keywords: composite material, tubular braided composite, open-mesh braided composite, finite element analysis, tensile test, micro-computed tomography, mechanical performances, geometrical model, periodic boundary condition, unit-cell model

Introduction

Composite materials contain two or more materials with different mechanical properties. The combination of these materials provides improved mechanical properties over the individual components [1]. Braided composites are a form of continuous fiber-based reinforced materials used in aerospace, automotive, petroleum, medical treatments, sporting, and marine applications [2-4]. For example, they can be used in hoses, pipes, or medical catheters to increase their performance [5]. Braided composites have significant advantages compared to conventional laminate composites. These advantages include out-of-plane stiffness, strength, toughness properties, net-shape fabrication, lower fabrication cost, and better impact and delamination resistance [6-7]. Because of these advantages, the studies that investigate braided composite and

their application are increasing significantly.

In two-dimensional braided composites, yarns are interlaced only in one plane and in two directions (clockwise and counterclockwise). The preform can be manufactured as either flat braided composite or Tubular Braided Composite (TBC) configurations. In addition, two-dimensional braided composites can be produced using a Maypole braider [8].

One way to categorize 2-D TBC is based on the pattern of yarns. Depending on the arrangement and movement of carriers, different patterns of braided composites are formed. The patterns of the braided composites are Diamond (one tow passing above and then below the other tows, 1/1), Regular (two tows passing above and then below the other tows, 2/2), and Hercules (three tows passing above and then below the other tows, 3/3). Different patterns of braided composites are shown in Figure 1.
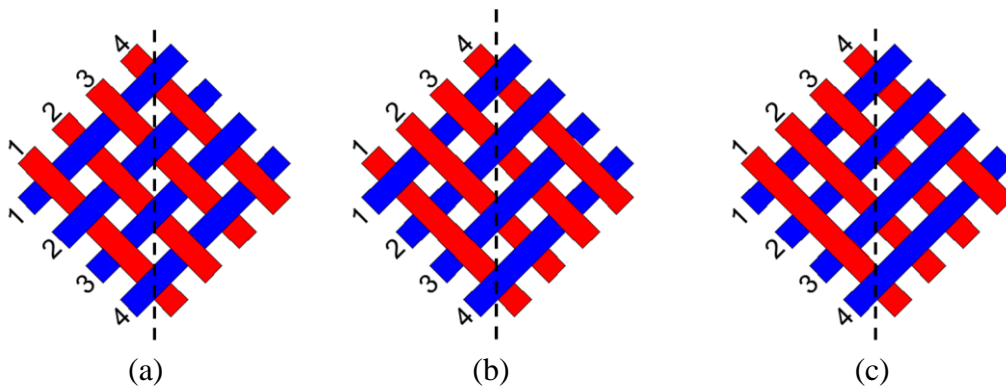

Figure 1 Different pattern of TBC's (a) Diamond (one by one), (b) Regular (two by two), and (c) Hercules (three by three),

The pattern shown in Figure 2 a) is known as the open-mesh Regular pattern, and Figure 2 b) shows a closed-mesh Regular pattern. There is a space between yarns in open-mesh TBC, while in the closed-mesh TBC, yarns contact each other. While closed-mesh TBC's are more frequently used in industry, open-mesh TBC's are used in the medical field as braided catheters and stents because the size of the stents should be as small as possible to prevent discomfort and provide easier manipulation [8,2,9]
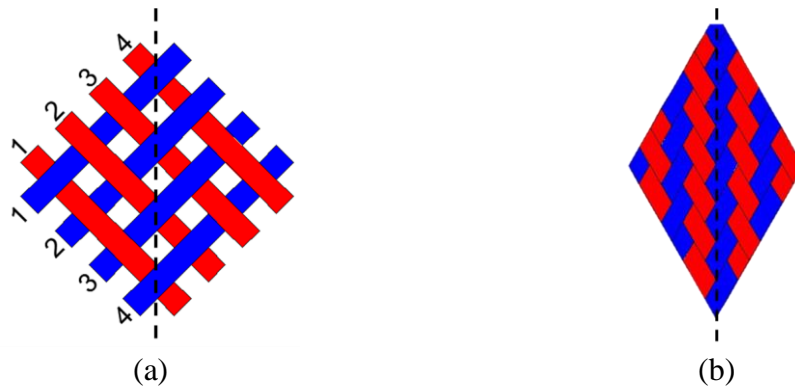
Figure 2 A Regular patter of TBC a) open mesh, b) closed-mesh

Several studies have provided mathematical models for TBC. Liao and Adanur [10] developed an external and an internal 3-D circular braid model. They used a Frenet frame technique for sweeping the cross-section over the yarn path. Rawal and Potluri [11-12] developed an algorithm to produce 3-D braided preforms over different mandrel cross-sections; cylinder, square prism, cones with circular and elliptical cross-section, and square pyramid. In their model, the yarn paths are modelled as straight lines and undulations are ignored. Gholami and Melenka [13] developed an algorithm for generating a yarn path and solid model for TBC. Alpyildiz [14] proposed a 3-D geometrical model for tubular braids. In this research, the braiding yarn's crimp is considered together with the tubular curvature of the tubular braided structure in the model. The provided model worked with different braid structures, braid angle, the number of yarns in a set, yarn, and mandrel diameter. Rawal et al. [15] developed geometrical models in cylindrical and conical mandrels with Diamond, Regular and triaxial forms. They used the Virtual Reality Modelling Language (VRML) to simulate the model. Finally, the geometrical models were verified by visually comparing them with camera images of actual models. One of the issues in the models developed in [11]–[15] is that the orientation of the ridges in TBC is assumed to be perpendicular to the axis of the TBC. However, as explained in [16], manufacturing such a TBC is not possible with conventional braiding machines. Therefore, the models should be edited

to produce TBC's with ridges orientation parallel to the TBC's axis.

In the papers introducing the geometrical model of TBC, the proposed models are not compared against physical braid samples to study the relevant error and the effect of the existing assumptions. Ning et al. [17] provided a geometrical model for TBC using the generalized rose curve. They generated their model in different mandrel shapes and compared their cylindrical geometrical model with an actual cylindrical TBC by comparing their images taken by a camera. However, the actual TBC they were comparing their result with were closed-mesh TBC, and they did not compare their results with an open-mesh TBC.

Having an accurate geometrical model of TBC is the primary step for having a precise and comprehensive simulation model to predict their mechanical properties. Geometrical equations for TBC must be accurate and easy to implement. In addition, geometrical models should be realistic enough to provide precise models simulating TBC's actual shape and behaviour. However, creating a geometrical model without assumptions is not possible. For the geometrical model in this paper, the following assumptions have been made [11]:

Assumption (1): The cross-section of the yarns is assumed to be circular with r radius.

Assumption (2): The yarns are solid and uncompressible. In the actual models, the cross-section of the yarns will change depending on the force applied to the TBC. However, since the yarns in this paper are assumed to be single, solid fiber, they are uncompressible.

Assumption (3): The braid paths do not slip and keep the constant sinusoidal pattern throughout the braid length. TBC are flexible in nature, specifically open-mesh uncured

TBC. Some yarns might shift from their ideal shapes when inserting an uncured open-mesh, TBC, into a mandrel. It can happen in the process of manufacturing the cured braid as well. However, the yarns stay in an ideal path in the geometrical model and do not change their position.

The above assumptions consider TBC's overall characteristics; however, they ignore some specifications, such as the flexible nature of yarn paths and variable cross-section shapes. For having a real-shape model, considering all the details and characteristics of a real TBC, other methods like micro-Computed Tomography (μCT) can be used [16-17].

μCT is a non-destructive imaging method that can acquire high-resolution 3-D images (voxel size can be less than one micrometre). By using μCT, essential information of TBC is obtained. Bale et al. [20] statistically analysed the shape and positioning of fiber tow of two ceramic-matrix textile composites in the 3-D woven architecture. Melenka et al. [21] used μCT to analyze porosity/void in braided composites and extract geometrical parameters of yarns. Wang et al. [22] discussed the microstructure of 3D braided composites and provided a modelling approach based on the Free Form Deformation (FFD) theory. Melenka et al. [23] used high-resolution μCT to identify the fibers of yarns in a 2D TBC.

Different studies have been done to study the behaviour of braided composite by using the FEM method [24–30]. Lomov et al. [31] developed meso-FE modelling for textile composite. They provide a road map for creating a mesoscale model for obtaining mechanical properties, studying the stress-strain field, and simulation of damage present in the textile composite within a unit cell. Finally, they compared the developed meso-FEM with Chamis' analytical model [32] and experimental results. The FEM results

show closer results to experimental results compared to the analytical model. The WiseTex software package [33] was used for generating the geometrical model, which does not support generating TBC. As a result, the simulation of TBC is not considered in this study.

Xu et al. [34] analyzed flat braided composite by FEM. They modelled braided composite with different braid angles and studied braid angle's effect on braided composite mechanical properties. They considered unit cells in each case and applied Periodic Boundary Condition (PBC) for their model. Zhang et al. [35] used the FEM method to simulate braided composite tubes to study the energy absorption of braided composites to improve the crashworthiness of components. In their research, the cross-section of each yarn is assumed to be rectangular and remains constant along the entire yarn path. Also, the axial yarns were assumed to be completely straight, and braiding yarns were considered to follow a straight path. Finally, simulated results were validated by comparing them with experimental test results.

Wang et al. [36] provided a FEM analysis based on a geometrical model. They created a rectangular braided composite by TexGen software, an open-source software package, and used a mapping method to convert the rectangular model into a tubular form. Zhang et al. [37] developed a mesoscale voxel-based FEM for analyzing the effect of the voxel size on the 3D angle-interlock woven composites subjected to axial tensile loading.

In this paper, a new FEM model for braided composites is introduced. The TBC-Gen program for generating geometrical TBC models is utilized. TBC-Gen can produce yarn paths for all three yarn patterns with different variables. TBC-Gen was created using existing geometrical models from the literature. The program is developed in MATLAB software package, and the generated path will be imported into SolidWorks for creating

the solid model. A μCT scan was also performed for an open-mesh TBC, and the developed 3-D model is compared against the geometrical model generated by TBC-Gen and SolidWorks. Finally, a FEM based on the geometrical model for analyzing TBC's mechanical performance under the tensile test is developed. Also, the effect of braid angle and braid patterns on the displacement of the TBC is studied. The FEM results are compared against experimental and analytical results for validation purposes. The methodology presented in this manuscript will provide a method to understand the mechanical behaviour of TBC more thoroughly.

Method

Geometrical Models

The geometrical variables for generating a geometrical model are the number of yarns, braid angle, yarn diameter, mandrel diameter, length, or the number of turns of TBC. Some of the geometrical variables of a Regular braided composite pattern is shown in Figure 3. The indicated variables are braid angle (θ), yarn diameter (d), and undulation length. Braid angle is the most critical geometrical variable that significantly affects the mechanical properties of the TBC [38]. Other parameters of TBC and the process for developing each yarn pattern are introduced in Appendix 1.
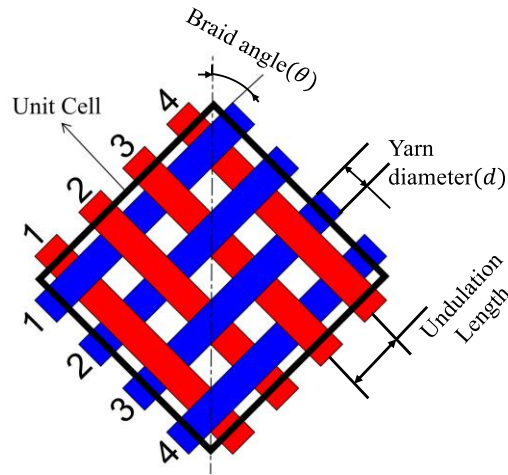
Figure 3 A unit cell of a Regular braided composite pattern showing geometrical variables

MATLAB Algorithms Used for Generating Yarn Patterns

For generating all the different patterns discussed in the previous sections, a custom-made program named TBC-Gen is designed in the MATLAB software package (R2020B, The MathWorks Inc, Natick, Ma, USA). The algorithm followed in this paper is shown in Figure 4. This algorithm starts by defining and importing geometrical values into the TBC-Gen, creating a solid model, and finally importing it into the FEM software package. The complete details for the TBC-Gen geometrical model are presented in Appendix 1.
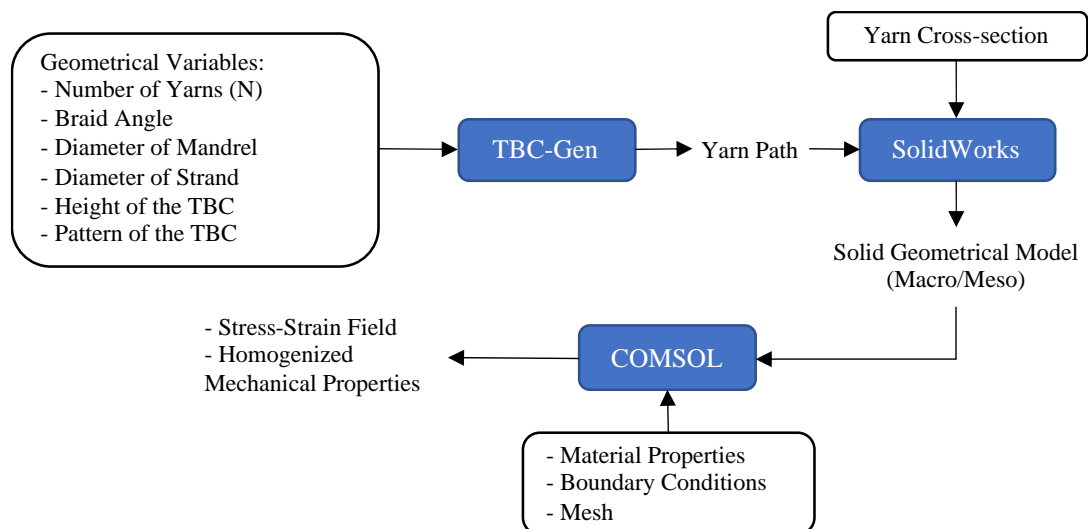
Figure 4 The flow chart of the algorithm followed in this paper.

The TBC-Gen needs five input geometrical variables to design the yarn path. Number

of yarns, braid angle (in degrees), the diameter of the mandrel in mm (inner diameter of the tubular braid, it should also be considered that the diameter of the mandrel is $2(R - 2r)$ in mm), the diameter of the strand $(2r)$ in mm, and the number of turns or height of the tubular braid in millimetres (only one of these two variables is required to be inputted, the other variable will be calculated based on the prescribed value). TBC-Gen can produce all three yarn patterns, i.e. Diamond, Regular, and Hercules. The user can select to see the single path of clockwise or counterclockwise yarn or both simultaneously. As the user changes the parameters, the updated path will automatically be displayed in the plot section. Finally, the XYZ centre points of the designed yarn path for two counterclockwise yarns and two clockwise yarns, and a properties file including the input parameters, the designed pattern, and date and time, can be exported as five separated text files. Created clockwise or counterclockwise yarn paths can be uploaded and displayed in the TBC-Gen's display window. The XYZ values are also displayed in the program for control purposes. Alternatively, the generated properties file can be uploaded as well. By uploading the properties file, the program will scan and read the parameters and the pattern of the TBC path and change the program's setting accordingly.

Generating the Solid Geometrical Model

For creating the geometrical model by adding a cross-section to the designed yarn path in the previous section, the SolidWorks software (version 2020, Dassault Systèmes SOLIDWORKS Corp., Massachusetts, USA) is used. First, one clockwise and one counterclockwise yarn path generated in TBC-Gen is imported into SolidWorks. Next, the generated text file in the developed MATLAB program is imported into SolidWorks using the "Curve though XYZ Points…" function. After importing both yarn paths, two separate circular cross-sections are sketched in the XY plane. At the same time, the

circle's centre coincides with the yarn path. The cross-section sweeps the designed path and creates the yarn solid geometrical model using the "Sweep" function. Finally, using the "Circular Pattern," n number of yarns are patterned around the TBC's axis for each of the counterclockwise and clockwise directions (for Regular pattern, two sets of clockwise and two sets of counterclockwise yarn paths are generated. Therefore, $n/2$ of yarns are patterned around the TBC's axis).

Micro-computed Tomography (μCT)

μCT is considered a microscopic version of clinical Computed Tomography (CT). For generating 3-D models out of a μCT, the testpiece will rotate around its axis with a predefined step size. The smaller the step size, the more accurate results. Because of the cylindrical shape of the TBC, only half of the TBC (180°) is required to be scanned. The 2-D images are combined and result in a stack of cross-sectional 2-D images. By sticking these 2-D cross-sectional images, a 3-D model of the testpiece is created [39], as shown in Figure 5. In Figure 5, the X-ray tube produces X-rays and send them toward the test piece. Then the X-ray CCD (Charge Coupled Device) detector captures the X-rays passing the test piece. A motor controls the rotation step of the test piece for taking images in different rotations. All the acquired images are transferred to a computer for further image processing.
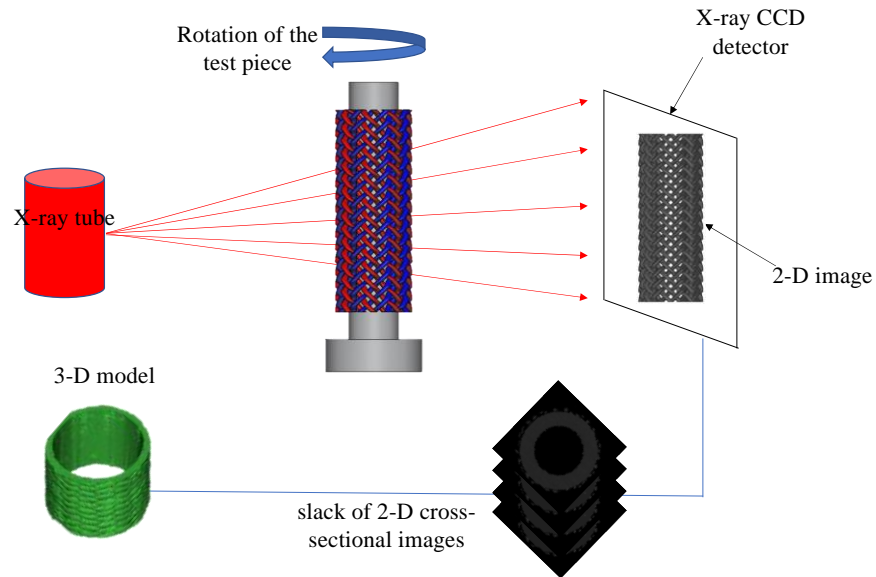
Figure 5 μCT component used for scanning a Tubular Braided Composite.

In this study, the TBC's were examined using a desktop μCT scanner (SkyScan 1272, Bruker-MicroCT, Kontich, Belgium). The μCT settings for this scan are tabulated in Table 1. An open-mesh, dry (no resin) Kevlar 49 fiber TBC with 48 yarns were used for this experiment. Also, ten different measurements were done at different points of the TBC. The average value for braid angle was 40.53°(with a 5.75° standard deviation), and the average value of yarn width was 0.88 mm (with a 0.14 mm standard deviation). Braid angle and yarn thicknesses were measured by analyzing images taken directly from TBC with a camera and using ImageJ software (National Institutes of Health, USA). Because of the open-mesh TBC's flexible nature, some yarns are distorted and do not stay in their ideal shape. As a result, they do not have a consistent braid angle through the yarn path. A specific 20 mm, hollow cylinder mandrel, is 3D printed to hold the TBC, and a 5 mm steel mount is inserted at the bottom of the mandrel, shown in Figure 6 a). The measured yarn width and braid angle are shown in Figure 6 b). The created cross-section after analyzing all of the μCT images is shown in Figure 6 c). 1533 images were taken from scanning 180° of the TBC. By multiplying the number of images to the resolution of the scan (10.88 μm), the height of the scanned TBC would

be 16.68 mm. To remove the mandrel from the cross-section, a circular subtractive region of interest is defined within the mandrel cross-section. The resulting cross-section is shown in Figure 6 d). Next, the cross-section images are binarized to increase the contrast between the background and yarns. By doing so, the yarn detection process would be more straightforward. As shown in Figure 6 e), the mandrel diameter is measured by fitting a circle into the inner side of the cross-section.
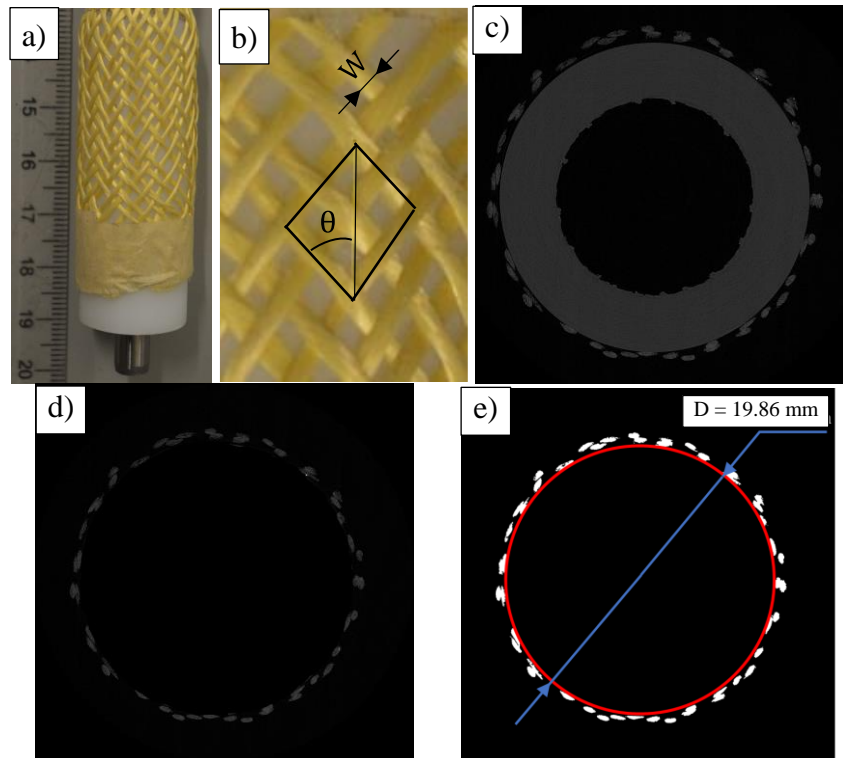

Figure 6 a) The tested TBC inserted into the mandrel next to a ruler, b) measuring the actual geometrical variable of TBC by evaluating the image in ImageJ software, c) the μCT result of the cross-section of the scanned TBC, d) removing the mandrel by defining a subtractive region on interest mask, and e) binarized cross-section and measuring the mandrel diameter in ImageJ software

Table 1 The setting of the μCT experiment

μCT parameters	Value
Image pixel size	10.88 μm
Source Voltage	55 kV
Source Current	166 μA
Number of scanned Images	1533
Exposure	1876 ms
Rotation step	0.1°
Rotation angle	180°
Frame Averaging	4
Duration	4 hour and 35 minutes

The 2D images taken by μCT were imported into NRECon software (NRECON 1.7.1.0, Bruker, Belgium) to reconstruct the 2D cross-sectional images like the image shown in

Figure 6 c). These images are 8-bit bitmap (BMP), and the size of the created images were 2452 × 2452 pixels. A 3-D model of the scanned TBC is generated after importing the cross-section images into CTAn software (Bruker-MicroCT, Kontich, Belgium). The result is shown in Figure 7 a). Also, the virtual geometrical model of the scanned TBC is generated by the TBC-Gen, and SolidWorks and is shown in Figure 7 b) for comparison with the μCT model.
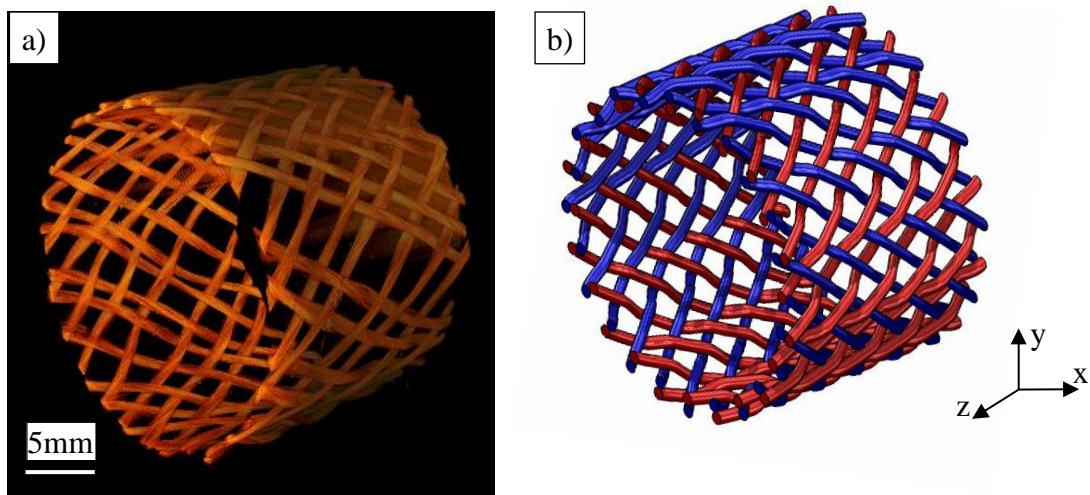
Figure 7 a) The 3D result model of the TBC generated by CTAn software, b) the generated geometrical model using the TBC-Gen program.red: counterclockwise, blue: clockwise

For analyzing the yarn cross-sections, image processing algorithms of MATLAB are used. First, the binarized images are scanned using "bwboundaries" function. The scanned cross-section image and the detected yarn boundaries are shown in Figure 8 a). A closer view of six yarn cross-sections with their calculated area is shown in Figure 8 b). By detecting the yarn boundaries, other parameters of the yarns like major and minor diameters, area, orientation, and the centre are obtained, which are shown in Figure 8 c). The major and minor diameters of the detected boundary are major and minor diameters of an assumed ellipse fitted to the detected cross-section boundary. Also, the boundary orientation is the angle between the major diameter and horizontal axis of the yarn, in

degree.
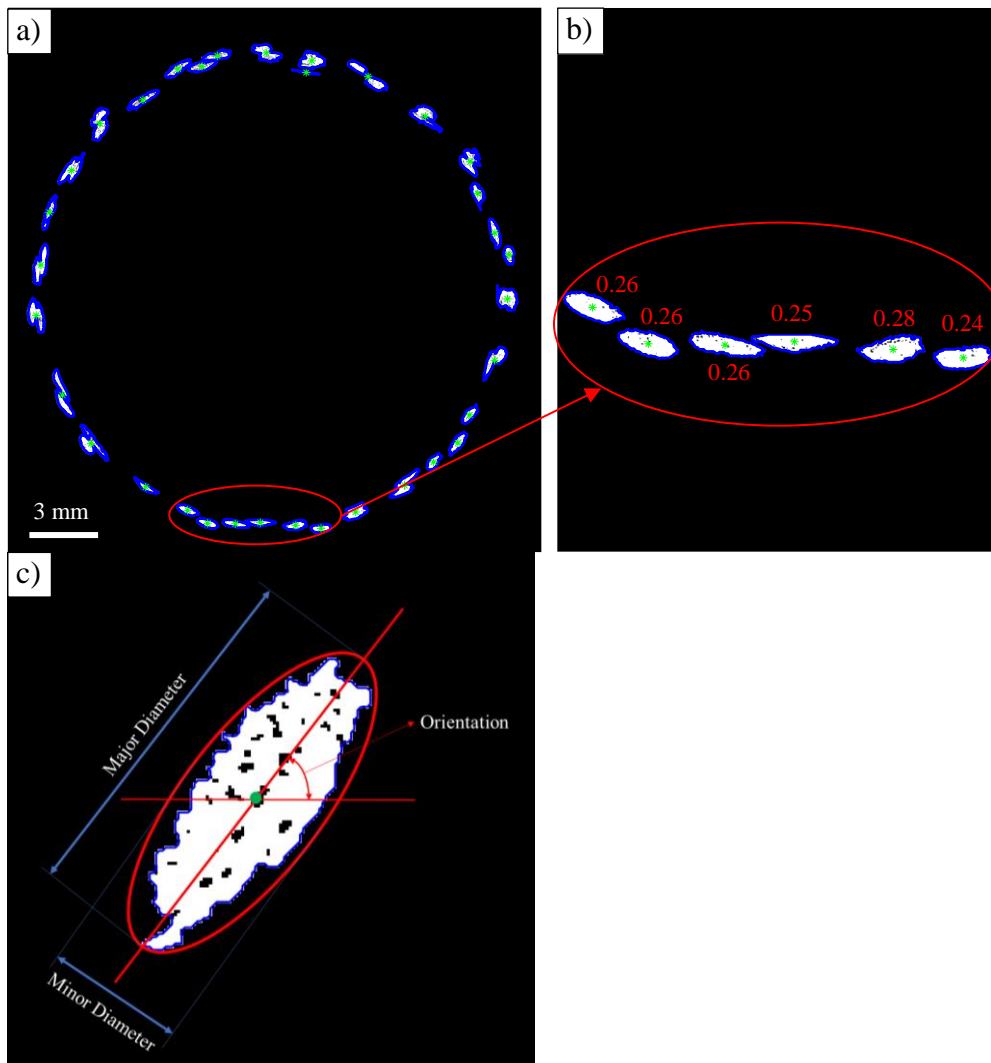
Figure 8 a) Detected boundaries of yarn cross-sections, b) six detected yarn boundaries, the centre of yarns, and the area of yarn cross-section (mm^2), and c) a detected yarn cross-section showing major and minor diameters, yarn canter, and orientation in MATLAB software

Finite Element Modelling

The constitutive behaviour of complex material like TBC can be studied either by experimental tests or numerical simulation. TBC can be studied at three hierarchical structural levels; macro, meso, and micro levels [31]. The macro-level consists of the overall geometry of the TBC material. The global condition at the macro-scale refers to the complete loading condition of the TBC. The micro-scale deals with the arrangement of the fibers in the impregnated yarn. Local properties on a micro-scale refer to the actual properties of fiber and matrix. The size and mechanical properties of the

mesoscale is between the macro-scale and micro-scale. In other words, the local

properties on mesoscales refer to global properties on a micro-scale. Also, the global

properties in mesoscale refer to local properties on a macro-scale [31]. A sample of

micro-scale, mesoscale and macro-scale models of a TBC is shown in Figure 9. For the

FEM of the TBC, it is assumed that the fibers are perfectly bonded to the matrix [40].
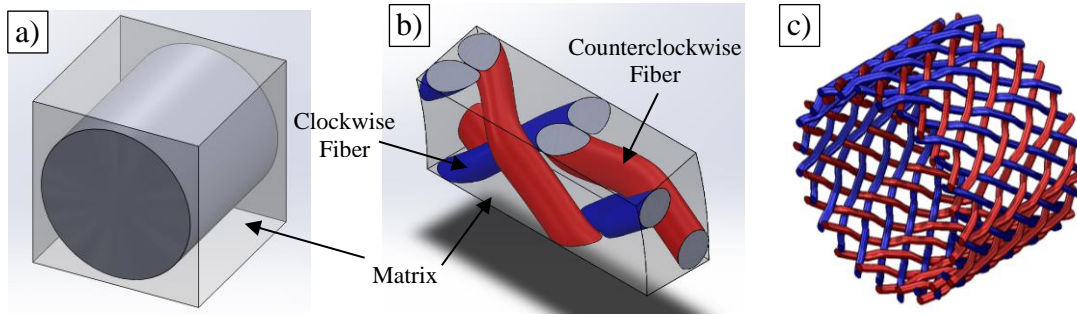
Figure 9 a) micro-scale, b) mesoscale, and c) macro-scale models of tubular braided composite crock wise (red) and counterclockwise (blue)

For generating the FEM, a geometrical model of an open-mesh Diamond TBC with 18

yarns, 30° braid angle, 24.71 mm inner diameter (diameter of the mandrel), 1.51 mm

strand diameter, and 30 mm length is designed. The matrix is added to the designed

geometry. The thickness of the matrix is intended to be more than the fibers to prevent

zero thickness when generating the geometrical model and meshing step. As a result,

the inner diameter of the matrix is 24 mm. The macro-scale and the mesoscale (40°

cross-section of the complete model, $2\pi/n$) models are shown in Figure 9 a) and Figure

9 b), respectively. The designed model is imported into the FEM software package

(COMSOL Multiphysics 5.5, Stockholm, Sweden) for analysis.

Periodic Boundary Conditions

Periodic Boundary Condition (PBC) is a set of boundary conditions used for evaluating

a large component only by solving a small part of the problem (unit cell). Assuming the

unit cell is characterized by a transition vector $(\vec{b_1})$ as shown in Figure 10 c), the

translation equation would be as (14).

$$A' = A + \vec{b_1} \tag{1}$$
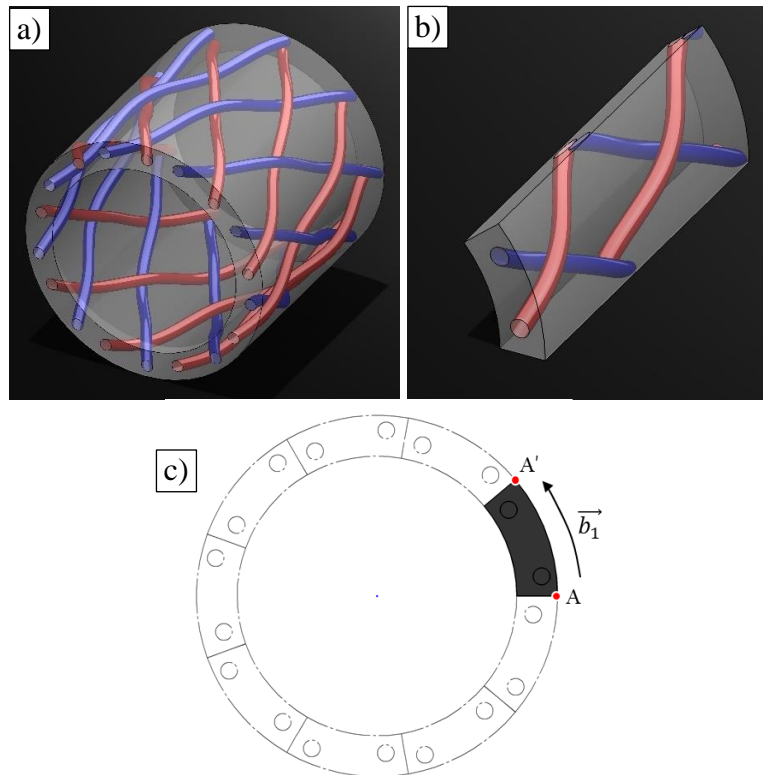
Figure 10 The geometrical designed model with 18 yarns, 30° braid angle, 24.71 mm inner diameter, 1.51 mm strand diameter, and 30 mm length. a) macro-scale model, b) mesoscale model

In COMSOL, the boundary condition expressed in (1) can be applied by choosing cyclic symmetry under the periodic boundary condition. One important point for using PBC is keeping the meshes' consistency which COMSOL automatically considers this point into account. One method for manually controlling the consistency of the meshing is copying the nodes from one side of the unit cell to the other side, then meshing the area between these two surfaces. In this case, the meshes on both sides of the unit cells are identical [31].

The imported model into COMSOL software under the tensile test is shown in Figure 11. The yarn material is assumed to be Kevlar 49 fiber, and for the matrix Epon825/Ancamine 1482 resin. The properties of both materials are tabulated in Table 2.
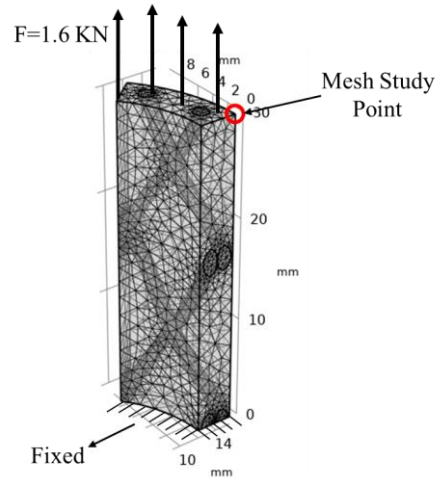
Figure 11 Imported mesoscale geometrical model into COMSOL software after meshing, under tensile test, and after applying PBC

Table 2 properties of the material used in FEM [41]

Kevlar 49 fiber		Epon825/Ancamine 1482 resin	
$\{E_1, E_2, E_3\}$	$\{130, 7.3, 7.3\}$ (GPa)	E	3.5 (GPa)
$\{G_{12}, G_{23}, G_{13}\}$	$\{2.86, 6.89, 2.86\}$ (GPa)	v	0.3
$\{v_{12}, v_{23}, v_{13}\}$	$\{0.35, 0.35, 0.35\}$	ρ	$1100\ (Kg/m^3)$
ρ	$1800\ (Kg/m^3)$		

Free tetrahedral mesh is used for analyzing the model shown in Figure 11. However, for finding the optimum size of the mesh, a mesh study is required. Therefore, nine mesh categories are used for analyzing the mesoscale model represented in Figure 11. The mesh categories start from coarse to fine. The number of elements (NO_e), maximum element size (max_e), minimum element size (min_e), maximum element growth rate (growR), curvature factor (ResCurv), and resolution of narrow regions (ResNar) are parameters of each category which are tabulated in Table 3.

Table 3 Parameters of each mesh category used for the mesh study

Mesh Category	Extremely course (1)	Extra course (2)	Coarser (3)	Coarse (4)	Normal (5)	Fine (6)	Finer (7)	Extra fine (8)	Extremely fine (9)
NO_e	2313	3013	4552	10284	29519	65008	182757	388722	942064
max_e	10.7	6.39	4.05	3.2	2.13	1.7	1.17	0.746	0.426
min_e	1.49	1.15	0.852	0.597	0.384	0.213	0.0852	0.032	0.00426
growR	2	1.85	1.7	1.6	1.5	1.45	1.4	1.35	1.3
ResCurv	1	0.9	0.8	0.7	0.6	0.5	0.4	0.3	0.2
ResNar	0.1	0.2	0.3	0.4	0.5	0.6	0.7	0.85	1

Three outputs are captured at the mesh study point using each mesh category shown in Figure 11: the von Mises stress, the first principal stress, and the displacement. A 1.6 KN force is applied to the upper side of the model alongside the TBC. The actual

recorded values of each mesh category and their relevant percentage differences are plotted separately and are shown in Figure 12. The percentage difference is calculated as (the value of mesh size (2) − the value of the mesh size (1)) / the value of mesh size (1).
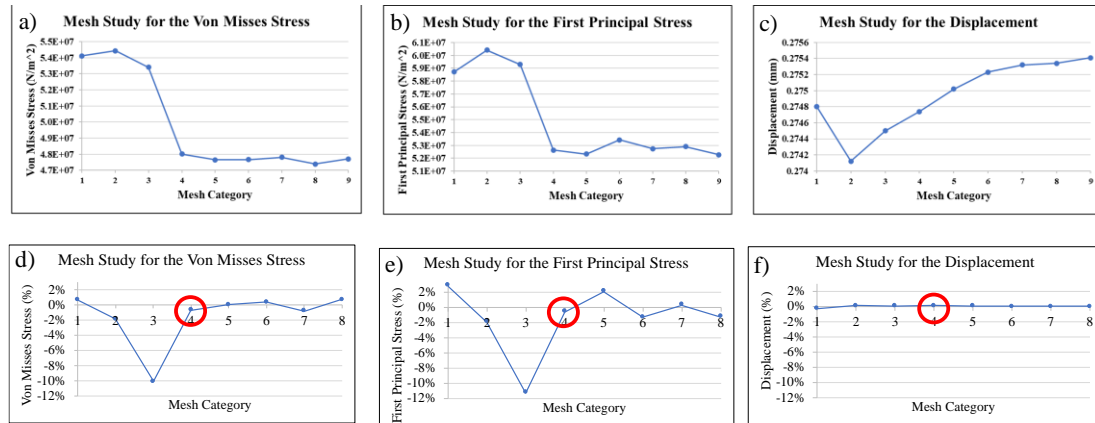
Figure 12 Mesh study on a mesoscale model at one point under tensile test. a) mesh study result for von Misses stress, b) mesh study result for first principle stress, c) mesh study result for displacement, d) percentage difference between Von Misses results in different mesh sizes, e) percentage difference between First Principal stress results in different mesh sizes, f) percentage difference between Displacement results in different mesh sizes.

For Von Misses stress, after category 4 (coarse mesh), the stress value does not change significantly, and the difference is below 1%. For the first principal stress, the stress values converge after mesh category 4 (coarse mesh), and the percentage difference is below 2%. Finally, in all the mesh categories, the percentage difference is below 0.25% for the displacement. As a result, category mesh 4 (coarse mesh) will provide enough accurate results for this study, and finer mesh will refine the results by less than 2%. At the same time, it would be more computationally expensive.

Results

Geometrical Model

A sample of TBC solid geometrical model from each TBC pattern (Diamond, Regular, and Hercules) with similar geometrical parameters are generated using TBC-Gen and SolidWorks. The inputted parameters are Number of yarns = 32, Yarn radius =

0.5 mm, Mandrel radius $= 10\ mm$, Braid angle $= 45°$, and length of TBC $= 50$ mm. The generated solid models are shown in Figure 13.
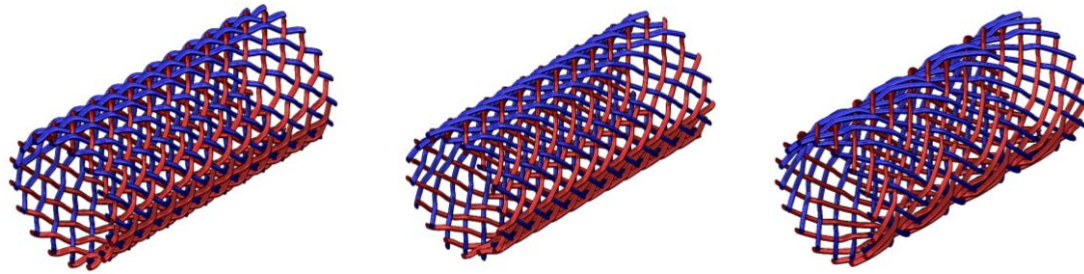
a) Diamond	b) Regular	c) Hercules
N = 32	N = 32	N = 32
r = 0.5 mm	r = 0.5 mm	r = 0.5 mm
R = 10 mm	R = 10 mm	R = 10 mm
$\alpha = 45°$	$\alpha = 45°$	$\alpha = 45°$
L = 50 mm	L = 50 mm	L = 50 mm

Figure 13 3-D solid model of a TBC, red: counterclockwise, blue: clockwise a) Diamond pattern, b) Regular pattern, and c) Hercules pattern

For validation of the developed geometrical model in this paper, a Regular TBC with Number of yarns = 16, Braid angle = 35°, Mandrel radius = 10 mm, Yarn radius = 0.5 mm, and length of the TBC = 98.7 mm is designed in both the TBC-Gen and a commercial software package, TexMind Braided software [42]. The output results of the two software are shown in Figure 14. The visual comparison between the two models shows a good agreement between them.

a)

b)
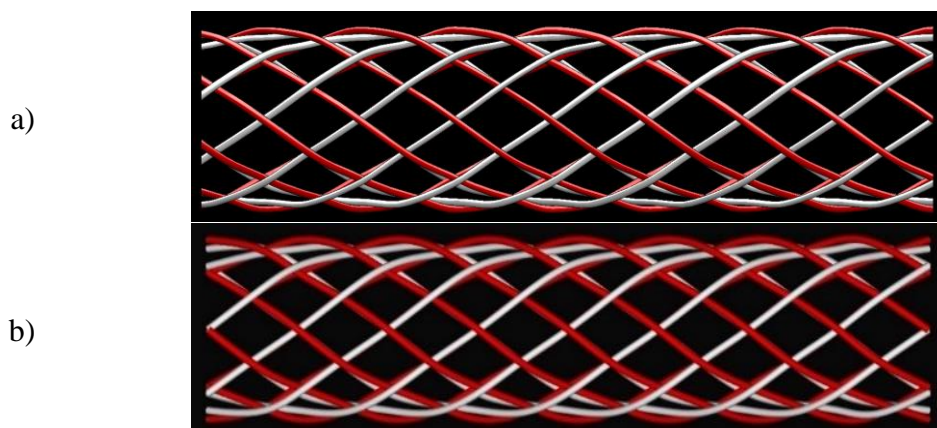
Figure 14 Comparing the result of the generated geometrical TBC model designed by the algorithm developed in this paper a), with the results of the same TBC designed in TexMind Braided software commercial software b). ($N =$ 16, $\alpha = 35°$, $R = 10.5$ mm, $r = 0.5$ mm, and the length of the TBC $= 98.7$ mm)

The TBC-Gen can generate yarn paths as X, Y, Z coordination points. Then this yarn

path will be imported into SolidWorks software to add a cross-section. This cross-section can be in various shapes. While in the TexMind software, the only cross-section is circular. Also, in the TBC-Gen, the composite material can be modelled in SolidWorks software by adding a matrix to the designed TBC.

Micro-computed Tomography (μCT)

The cross-sectional images shown in Figure 8 demonstrate the process for detecting the yarn cross-sections and obtaining other data of a TBC. By analyzing all the cross-sectional images and detecting yarn cross-section boundaries, some valuable data of the yarns can be extracted. The average value of major diameter for all the single yarn cross-sections is 1.078 ± 0.222 mm. Also, the average value of 10 measurements of the actual TBC using a camera and ImageJ software reveals the major diameter of 0.887 ± 0.146 mm. The measured major diameters and the relevant SD are shown in Figure 15. However, the μCT measured major diameter of yarns is showing bigger value compared to the measured major diameter using the camera. One reason for this difference is the curvature of the TBC. Since the camera measurements are based on a single image taken in the longitudinal direction of the TBC, the measured values will be smaller than the actual diameter. However, the μCT measurements are based on the cross-sectional images of the TBC, which consider curvature as well. Additionally, the camera measurements are the mean of 10 measurement samples. However, the μCT measurenments are representing the average value of all the single cross-sectional yarns. As a result, the μCT measurenments are more accurate.
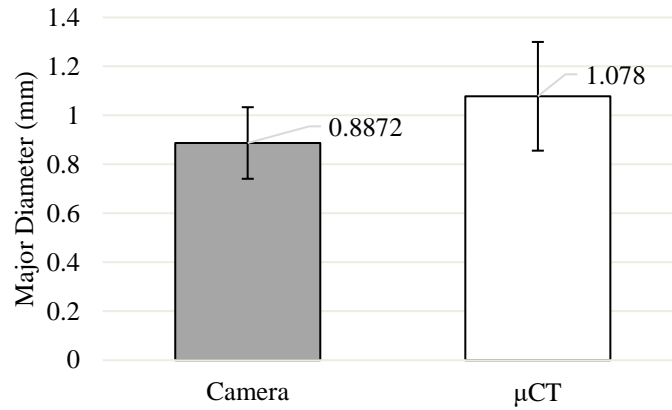
Figure 15 Major diameter of a TBC measuring by a camera and $\boldsymbol{\mu}$CT

The average value of the cross-section area of the scanned TBC is 0.2803 ± 0.0386 mm^2. To achieve an equivalent cross-sectional area, the relevant radius resulting in the same area with a circular cross-section is 0.3 mm. This radius can be used in TBC-Gen to generate the solid geometrical model that can be used for FEM analysis. The average value of the minor diameter of the scanned TBC was 0.3631 ± 0.0523 mm.

By visually comparing the virtual simulated model with the μCT model in Figure 7, the assumptions made for developing the simulation model are apparent. As one can see, the yarns in actual open-mesh TBC are not located in their ideal location, and some are significantly distorted. Additionally, the cross-section of yarns in the simulated model is assumed to be incompressible and circular, which is not entirely similar to the μCT results. However, the overall shape of both models is identical. For better comparison, a quantitative comparison between two models is required to be done in further studies. For making this quantitative comparison, all the cross-section images of the selected yarn should be scanned. After extracting the data of boundary, centre points, and the area of the yarn cross-section, they can be compared against the geometrical yarn path generated by TBC-Gen.

Finite Element Modelling

The Effect of Braid Angle on Displacement

This section will evaluate seven models with similar geometries and mechanical properties but different braid angles. The displacement of each model will be recorded and compared against each other. The braid angles range from 30° to 60° with a five-degree incremental step. The mechanical properties of fiber and matrix are according to Table 2, and the applied force is 12.5 KN in the Z direction. Other geometrical variables of the TBC are similar to the TBC shown in Figure 11. Three FEM results ($\theta = 30°$, $\theta = 40°$, $\theta = 60°$) out of seven cases are shown in Figure 16.
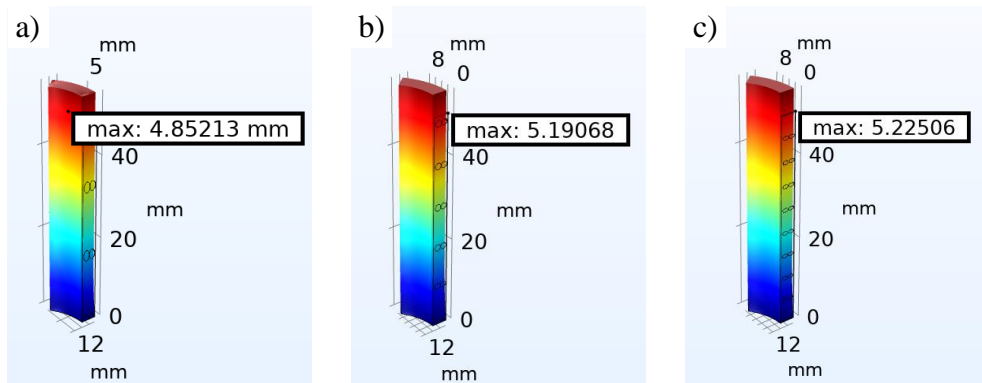
Figure 16 Displacement of Diamond tubular braided composite with $N = 18$, $R = 12.35\ mm$, $r = 0.75\ mm$ with braid angles between 30° to 60° under 12.5 KN tensile load. a) $\theta = 30°$, b) $\theta = 45°$, c) $\theta = 60$

The displacement value of all seven cases and the trending line is shown in Figure 17. As one can see, by increasing the braid angle, the longitudinal strength of the braid decreases, and as a result, the displacement of the TBC increases.
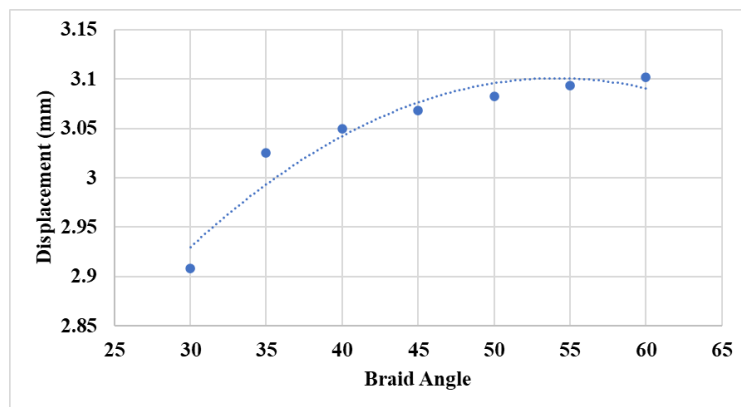
Figure 17 The effect of changing the braid angle on the displacement of the TBC

The Effect of Yarn Pattern on Displacement

Three geometrical models with similar geometrical variables but different yarn patterns,
as shown in Figure 13, are imported into COMSOL. A tensile test is designed for braid
patterns, and PBC and a 12.5 KN longitudinal force is applied. The material of the
fibers is assumed to be Carbon fiber, and the matrix is Epson 825/Ancamine 1482 resin.
The mechanical properties of fiber and matrix are tabulated in Table 4. The lower part
of the TBC is constrained by roller boundaries.

Table 4 Properties of fiber and matrix used for the experimental test, analytical model, and FEM [41]

	$E_{f11}(GPa)$	$E_{f22}(GPa)$	$G_{f11}(GPa)$	$v_{f11}(GPa)$
Kevlar 49 fibers	130	7.3	2.86	0.35
Carbon fiber	220	13.8	9.0	0.2
S2-glass	96.5	96.5	39.2	0.23
	E_m (GPa)		G_m (GPa)	v_m (GPa)
Epson 825/Ancamine 1482 resin	3.5		1.3	0.3

The displacement in the Z direction of each braid pattern is calculated and shown in
Figure 18. The figure shows that the maximum displacement in the Z direction in
Diamond is 0.8118 mm, Regular 0.8104 mm, and Hercules = 0.8098 mm. Also, the
location of the maximum displacement is in the top surface of the TBC. Thus, diamond
patterns are showing maximum displacement compared to two other patterns. It is
because of the one-by-one woven structure of Diamond that is causing less longitudinal
stiffness.

a) max displacement:
0.8118 mm

b) max displacement
0.8102 mm

c) max displacement:
0.8098 mm
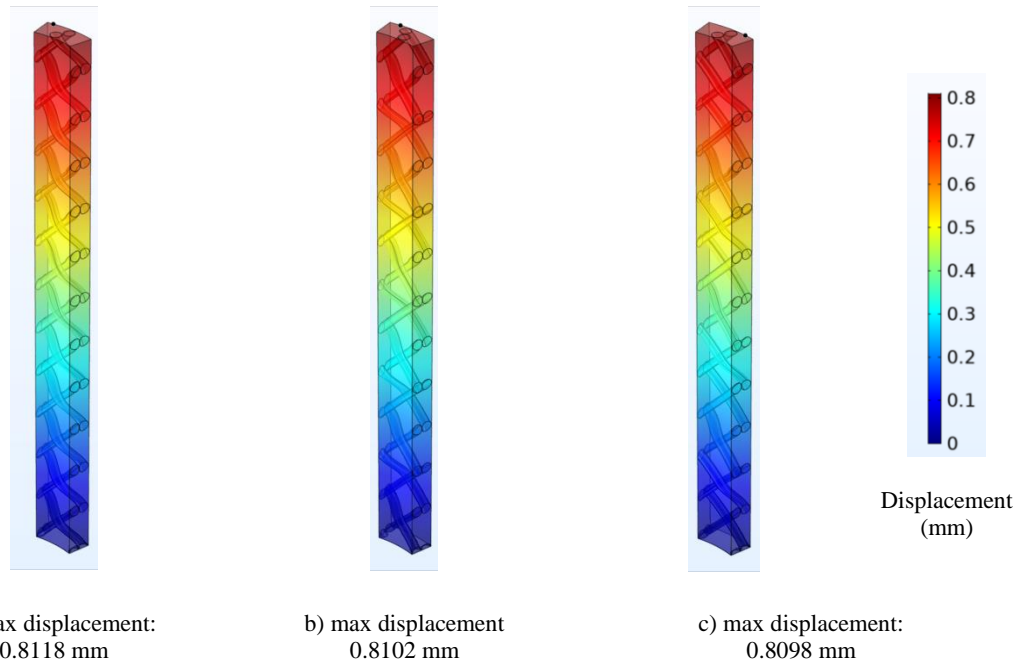
Figure 18 Tensile test of three carbon fiber TBC's with different yarn patterns under 625 N longitudinal force. a) Diamond, b) Regular, and c) Hercules

Validation

For Validation, the longitudinal modulus (E_{xx}) of three TBC with different geometry and material properties are calculated by the FEM and compared against the tensile experiment and analytical results reported in [41]. The material of three fibers is Kevlar 49 fibers, Carbon fibers, and S2-glass fibers. The matrix is also Epson 825/Ancamine 1482 resin.

For the experimental test, five samples of the Kevlar fibers and Carbon fibers, and four samples of S2-glass were prepared. The average dimensions of the samples are tabulated in Table 5.

Table 5 Average geometry of the three used TBC's [41]

	Number of Yarn (N)	Diameter of Mandrel (mm)	Braid angle (deg)	Diameter of yarn (mm)
Kevlar 49 fibers	18	24.71 ±0.28	44.19 ±1.63	1.51 ±0.15
Carbon fiber	18	24.54 ±0.19	41.80 ±0.11	1.58 ±0.09
S2-glass	18	24.53 ±0.47	46.00 ±1.30	1.48 ±0.04

The experimental longitudinal modulus was measured from a tensile test. The Curved-model based on Classical Laminate Plate Theory (CLPT) was used to predict the

analytical results for each case. In modelling the FEM, a predefined displacement was applied to the TBC model. Then, the relevant stress and strain were calculated accordingly. The mandrel and yarn diameters were considered constant for each sample, and the reported average value was used for them. However, the three braid angles (the nominal braid angle, the maximum braid angle, and the minimum braid angle as tabulated in Table 5.) were used for generating solid models and estimating the value and standard deviation of the E_{xx}. Since $n = 9$, 1/9 ($2\pi/9 = 40°$) of the complete TBC was used to model the FEM, and the PBC was applied to that partial model. E_{xx} was calculated by dividing the values of stress by strain.

In the experimental test, the E_{xx} was also calculated as the slope of the stress-strain curve, and the test was repeated for all the samples. For Kevlar 49 TBC, the average value of the experimental E_{xx} was 2.85 ± 0.49 GPa, and for the Curved model, it was 4.15 ± 0.67 GPa. The difference between the experimental and analytical models is 46%. The FEM reported $E_{xx} = 3.19 \pm 0.19$ GPA, which resulted in an 18% difference compared to the experimental results. For further comparison of the obtained values, a T-test [43] is applied to each comparison, and the Probability Value (P-value) of each comparison is reported in Table 6. The P-value between Experimental and FEM results for Kevlar 49 TBC is about 14%. As a result, it does not reject the null hypothesis, which means there is not a significant difference between FEM and Experimental results.

Table 6 P-Value of the estimated E_{xx}

Material of the TBC	Type of the test	FEM	Experiment
Kevlar 49 fiber	Experiment	0.1415	
	Curved Model	0.1376	0.0565
Carbon fiber	Experiment	0.2582	
	Curved Model	0.0024	0.0027
S2-glass	Experiment	0.0013	
	Curved Model	0.0154	0.0005

The estimated values of the Curved model for E_{xx} of Carbon fiber is 8.88 ± 1.35 GPa,

and the reported experimental value is 3.03 $\pm$0.77 GPa. The error between analytical and experimental values for Carbon TBC is 193%. The FEM E_{xx} value for Carbon fiber TBC is 3.61 $\pm$0.015 GPa which shows a 19% error compared to the value of the experimental test for Carbon fiber. Also, the T-test P-value between Experimental and FEM values is 26%, not rejecting the null hypothesis. Therefore, there is no significant difference between the two values.

Finally, the reported experimental value for E_{xx} of S2-glass fiber is 1.44 $\pm$0.11 GPa, and the analytical Curved model result is 6.41 $\pm$0.82 GPa. The error between the Curved model and experimental result is 345%. However, the FEM reported 4.11 $\pm$0.56 GPa for E_{xx} which results in a 185% error. The T-test P-value between Experimental and FEM values is almost 0%, and it rejects the null hypothesis. Therefore, there is a significant difference between FEM and Experimental results. This significant difference might be because of the assumed mechanical properties of S2-glass, which is to be isotropic. Also, the reported mechanical properties might not be accurate.

As a result, there is no significant difference between FEM and experiment results for Kevlar 49 fiber and Carbon fiber material. For the S2-glass material, the result of FEM shows a minor error than the Curved model's result. The bar chart of tests for the three materials with their error bars is shown in Figure 19.
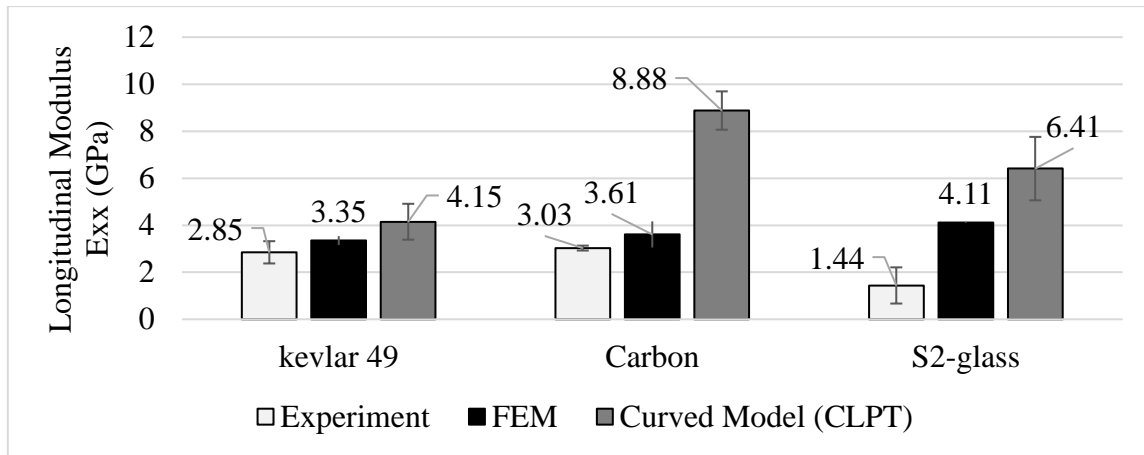
Figure 19 Comparing the results of experimental tensile tests for Kevlar 49 fiber, Carbon fiber, and S2-glass fiber with the relevant results of FEM and Curved-model

There might be several different sources contributing to an error in the FEM. One of the reasons might be the geometrical models used for the analysis. The geometrical model is made based on assumptions. For example, in actual open-mesh TBC's, the yarns are usually distorted from their location, as shown in Figure 7, while in the geometrical model, they are assumed to be in their ideal shape. Also, the cross-section of the yarns is changing throughout the yarn path in the actual model, while they are constant in the geometrical model. These assumptions add error to the model, and they can be reduced by using the actual geometrical model created by μCT method.

Conclusion

In this paper, the geometrical models for TBC patterns were introduced. Also, the process for generating these models using the TBC-Gen program developed in the MATLAB software package was explained. Finally, the generated yarn paths were imported into SolidWorks for adding cross-section and creating a solid model, which can be used for further analysis in FEM software packages.

Micro-Computed Tomography (μCT) was also used as a method for obtaining an accurate model of a TBC sample. A geometrical model with the same geometrical variables of the μCT scanned TBC was generated by using the TBC-Gen and was

visually compared with the resulted 3-D model of μCT. Also, the μCT measured yarn cross-section area can be used to create an equivalent area for the geometrical model.

A FEM was developed under tensile testing, and the effect of braid angle on the displacement was studied. It was seen that as the braid angle increases, the displacement increases respectively. Also, the effect of the braid pattern on displacement was studied, and the Diamond pattern showed the maximum displacement compared to the other patterns. A mesh study was carried out to choose the appropriate mesh size. Finally, the FEM tensile tests were simulated for three different materials. The resulted longitudinal modulus was compared against the experimental and analytical models by running a T-test. The FEM results were estimating the longitudinal modulus values more accurately than the analytical Curved model. The FEM model estimated the longitudinal modulus of Kevlar 49 fiber and Carbon fiber with 18% and 19% error, respectively.

The methodology represented in this manuscript will help to quickly design and analyze TBC's with different yarn patterns and geometrical variables for the desired application. Also, the represented μCT results show the potentials and accuracy of using this method for obtaining valuable geometrical variables. However, for having a quantitative comparison between μCT model and the geometrical model, more studies are required. It is expected that using μCT models for FEM will provide more accurate results.

Conflict of Interest

The author declares no conflicts of interest with respect to the research, authorship or publication of this article.

Data Availability Statement

The raw/processed data required to reproduce these findings cannot be shared at this time as the data also forms part of an ongoing study.

Supplementary Material

TBC-Gen program is available in the following address:

https://github.com/aligholamiYork/TBC-Gen

References:

[1]   A. K. Kaw, *Mechanics of composite materials*. CRC press, 2005.

[2]   C. Ayranci and J. Carey, "2D braided composites: A review for stiffness critical applications," *Compos. Struct.*, vol. 85, no. 1, pp. 43–58, Sep. 2008, doi: 10.1016/J.COMPSTRUCT.2007.10.004.

[3]   G. W. Melenka and J. P. Carey, "Development of a generalized analytical model for tubular braided-architecture composites," *J. Compos. Mater.*, vol. 51, no. 28, pp. 3861–3875, Dec. 2017, doi: 10.1177/0021998317695421.

[4]   J. Carey, A. Fahim, and M. Munro, "Design of braided composite cardiovascular catheters based on required axial, flexural, and torsional rigidities," *J. Biomed. Mater. Res.*, vol. 70B, no. 1, pp. 73–81, Jul. 2004, doi: 10.1002/jbm.b.30017.

[5]   Y. Kyosev, *Recent developments in braiding and narrow weaving*. Springe, 2016.

[6]   Z. M. Huang, "The mechanical properties of composites reinforced with woven

and braided fabrics," *Compos. Sci. Technol.*, vol. 60, no. 4, pp. 479–498, Mar. 2000, doi: 10.1016/S0266-3538(99)00148-7.

[7]   L. Xu, S. J. Kim, C.-H. Ong, and S. K. Ha, "Prediction of material properties of biaxial and triaxial braided textile composites," *J. Compos. Mater.*, vol. 46, no. 18, pp. 2255–2270, Aug. 2012, doi: 10.1177/0021998311431353.

[8]   J. P. Carey, *Handbook of advances in braided composite materials: Theory, production, testing and applications*. Woodhead Publishing, 2016.

[9]   F. K. Ko, "Braiding," *ASM Int. Eng. Mater. Handbook.,* vol. 21, 2001, doi: 10.1361/asmhba0003361.

[10]   Tianyi Liao and S. Adanur, "3D Structural Simulation of Tubular Braided Fabrics for Net-Shape Composites," *Text. Res. J.*, vol. 70, no. 4, pp. 297–303, Apr. 2000, doi: 10.1177/004051750007000403.

[11]   A. Rawal, P. Potluri, and C. Steele, "Prediction of Yarn Paths in Braided Structures Formed on a Square Pyramid," *J. Ind. Text.*, vol. 36, no. 3, pp. 221–226, Jan. 2007, doi: 10.1177/1528083707072354.

[12]   A. Rawal, P. Potluri, and C. Steele, "Geometrical Modeling of the Yarn Paths in Three-dimensional Braided Structures," *J. Ind. Text.*, vol. 35, no. 2, pp. 115–135, Oct. 2005, doi: 10.1177/1528083705057574.

[13]   A. Gholami and G. W. Melenka, "Generating Geometrical Models for Tubular Braided Composites," *CSME Conf. Charlottetown, PE, Canada*, 2021, [Online]. Available: https://library.upei.ca/islandora/object/csme2021%253A102.

[14]   T. Alpyildiz, "3D geometrical modelling of tubular braids," *Text. Res. J.*, vol. 82, no. 5, pp. 443–453, Mar. 2012, doi: 10.1177/0040517511427969.

[15]   A. Rawal, S. Gupta, H. Saraswat, and A. Sibal, "Geometrical modeling of near-net shape braided preforms," *Text. Res. J.*, vol. 85, no. 10, pp. 1055–1064, Jun. 2015, doi: 10.1177/0040517514559587.

[16]   Y. Kyosev, "Generalized geometric modeling of tubular and flat braided structures with arbitrary floating length and multiple filaments," *Text. Res. J.*, vol. 86, no. 12, pp. 1270–1279, Jul. 2016, doi: 10.1177/0040517515609261.

[17]   F. Ning, P. Potluri, W. Yu, and J. Hearle, "Geometrical modeling of tubular

braided structures using generalized rose curve," *Text. Res. J.*, vol. 87, no. 4, pp. 474–486, Mar. 2017, doi: 10.1177/0040517516632471.

[18] G. W. Melenka, B. M. Bruni-Bossio, C. Ayranci, and J. P. Carey, "Examination of voids and geometry of bio-based braided composite structures," *IOP Conf. Ser. Mater. Sci. Eng.*, vol. 406, no. 1, p. 012012, Sep. 2018, doi: 10.1088/1757-899X/406/1/012012.

[19] C. Unlusoy and G. W. Melenka, "Flexural testing of cellulose fiber braided composites using three dimensional digital image correlation," *Compos. Struct.*, vol. 230, Dec. 2019, doi: 10.1016/j.compstruct.2019.111538.

[20] H. Bale, M. Blacklock, M. R. Begley, D. B. Marshall, B. N. Cox, and R. O. Ritchie, "Characterizing Three-Dimensional Textile Ceramic Composites Using Synchrotron X-Ray Micro-Computed-Tomography," *J. Am. Ceram. Soc.*, vol. 95, no. 1, pp. 392–402, Jan. 2012, doi: 10.1111/j.1551-2916.2011.04802.x.

[21] G. W. Melenka, E. Lepp, B. K. O. Cheung, and J. P. Carey, "Micro-computed tomography analysis of tubular braided composites," *Compos. Struct.*, vol. 131, pp. 384–396, Nov. 2015, doi: 10.1016/j.compstruct.2015.05.057.

[22] Y. Wang, Z. Liu, N. Liu, L. Hu, Y. Wei, and J. Ou, "A new geometric modelling approach for 3D braided tubular composites base on Free Form Deformation," *Compos. Struct.*, vol. 136, pp. 75–85, Feb. 2016, doi: 10.1016/J.COMPSTRUCT.2015.09.036.

[23] G. W. Melenka and A. Gholami, "Fiber identification of braided composites using micro-computed tomography," *Compos. Commun.*, vol. 27, p. 100813, Oct. 2021, doi: 10.1016/j.coco.2021.100813.

[24] X. Ji *et al.*, "Multi-scale simulation and finite-element-assisted computation of elastic properties of braided textile reinforced composites," *J. Compos. Mater.*, vol. 48, no. 8, pp. 931–949, Apr. 2014, doi: 10.1177/0021998313480198.

[25] A. Shigang, Z. Xiaolei, M. Yiqi, P. Yongmao, and F. Daining, "Finite Element Modeling of 3D Orthogonal Woven C/C Composite Based on Micro-Computed Tomography Experiment," *Appl. Compos. Mater.*, vol. 21, no. 4, pp. 603–614, Aug. 2014, doi: 10.1007/s10443-013-9353-4.

[26] L. Zhang, D. Hu, R. Wang, Y. Zeng, and C. Cho, "Establishing RVE model

composed of dry fibers and matrix for 3D four-directional braided composites," *J. Compos. Mater.*, vol. 53, no. 14, pp. 1917–1931, Jun. 2019, doi: 10.1177/0021998318815735.

[27]   R. Wang, L. Zhang, D. Hu, and C. Cho, "Evaluation of three unit cell models in predicting the mechanical behaviour of 3D four-directional braided composites," *J. Compos. Mater.*, vol. 51, no. 27, pp. 3757–3767, Nov. 2017, doi: 10.1177/0021998317692657.

[28]   J. J. Gou, W. Z. Fang, Y. J. Dai, S. Li, and W. Q. Tao, "Multi-size unit cells to predict effective thermal conductivities of 3D four-directional braided composites," *Compos. Struct.*, vol. 163, pp. 152–167, Mar. 2017, doi: 10.1016/j.compstruct.2016.12.034.

[29]   K. Dong, J. Zhang, L. Jin, B. Gu, and B. Sun, "Multi-scale finite element analyses on the thermal conductive behaviors of 3D braided composites," *Compos. Struct.*, 2016, doi: 10.1016/j.compstruct.2016.02.029.

[30]   Y. H. Chen and M. H. Aliabadi, "Meshfree-based micromechanical modelling of twill woven composites," *Compos. Part B Eng.*, p. 108190, May 2020, doi: 10.1016/j.compositesb.2020.108190.

[31]   S. V. Lomov *et al.*, "Meso-FE modelling of textile composites: Road map, data flow and algorithms," *Compos. Sci. Technol.*, vol. 67, no. 9, pp. 1870–1891, Jul. 2007, doi: 10.1016/j.compscitech.2006.10.017.

[32]   C. C. Chamis, "Mechanics of composite materials: Past, present, and future," *J. Compos. Technol. Res.*, vol. 11, no. 1, pp. 3–14, Mar. 1989, doi: 10.1520/ctr10143j.

[33]   I. Verpoest and S. V. Lomov, "Virtual textile composites software WiseTex: Integration with micro-mechanical, permeability and structural analysis," *Compos. Sci. Technol.*, vol. 65, no. 15-16 SPEC. ISS., pp. 2563–2574, Dec. 2005, doi: 10.1016/j.compscitech.2005.05.031.

[34]   K. Xu, X. Qian, D. Duan, B. Chen, and L. Guo, "A novel macro-meso finite element method for the mechanical analysis of 3D braided composites," *Mech. Mater.*, vol. 126, pp. 163–175, Nov. 2018, doi: 10.1016/J.MECHMAT.2018.08.007.

[35]   P. Zhang, L.-J. Gui, Z.-J. Fan, Q. Yu, and Z.-K. Li, "Finite element modeling of the quasi-static axial crushing of braided composite tubes," *Comput. Mater. Sci.*, vol. 73, pp. 146–153, Jun. 2013, doi: 10.1016/j.commatsci.2013.01.026.

[36]   Y.-B. Wang, Z.-G. Liu, L. Hu, and Z. Wu, "Predicting the Elastic Modulus of 3D Braided Composite Tubes Using Geometrical Mapping Approach," *21st Int. Conf. Compos. Mater. Xi'an*, 2017.

[37]   D. Zhang *et al.*, "Finite Element Analysis of Mesh Size Effect of 3D Angle-Interlock Woven Composites Using Voxel-Based Method," *Appl. Compos. Mater.*, vol. 25, no. 4, pp. 905–920, Aug. 2018, doi: 10.1007/s10443-018-9723-z.

[38]   G. W. Melenka and C. Ayranci, "Advanced measurement techniques for braided composite structures: A review of current and upcoming trends," *J. Compos. Mater.*, vol. 54, no. 25, pp. 3895–3917, Oct. 2020, doi: 10.1177/0021998320903105.

[39]   J. D. Boerckel, D. E. Mason, A. M. McDermott, and E. Alsberg, "Microcomputed tomography: approaches and applications in bioengineering.," *Stem Cell Res. Ther.*, vol. 5, no. 6, p. 144, Dec. 2014, doi: 10.1186/scrt534.

[40]   D. Goyal, X. Tang, J. D. Whitcomb, and A. D. Kelkar, "Effect of various parameters on effective engineering properties of 2× 2 braided composites," *Mech. Adv. Mater. Struct.*, vol. 12, no. 2, pp. 113–128, 2005.

[41]   C. Ayranci, D. Romanyk, and J. P. Carey, "Elastic properties of large-open-mesh 2D braided composites: Model predictions and initial experimental findings," *Polym. Compos.*, vol. 31, no. 12, pp. 2017–2024, Dec. 2010, doi: 10.1002/pc.20999.

[42]   Y. Kyosev, "TexMind Software." http://texmind.com/wp/.

[43]   Student, "The Probable Error of a Mean," *Biometrika*, vol. 6, no. 1, p. 1, Mar. 1908, doi: 10.2307/2331554.

Appendix 1

Mathematical model of the tubular braided composites

Depending on the pattern of the braided composite (Diamond, Regular, and Hercules), there would be different equations to model them. However, all of them follow a helical path around the mandrel. As a result, they would have similar helical equations and curve with different undulation paths. Furthermore, there are two sets of yarns in braided composites, one counterclockwise (right-hand) and one clockwise (left-hand). Therefore, there would be two separate sets of equations with π phase shift difference between them for these models. For all the equations, X and Y represent the cross-section plane of the TBC. Also, Z represents the longitudinal axis of it (as shown in A-Figure 1).

The counterclockwise (right-hand) and clockwise (left-hand) helix's general equations for a yarn path around a cylindrical mandrel are shown in (A-1) and (A-2), respectively.

$$\begin{aligned} X_{ccw} &= R\cos\varphi \\ Y_{ccw} &= R\sin\varphi \\ Z_{ccw} &= R\,\varphi\cot\theta \end{aligned} \tag{A-1}$$

$$\begin{aligned} X_{cw} &= R\cos\varphi \\ Y_{cw} &= -R\sin\varphi \\ Z_{cw} &= R\varphi\cot\theta \end{aligned} \tag{A-2}$$

where X_{ccw}, Y_{ccw}, and Z_{ccw} are coordinate of points for a counterclockwise helix in X, Y, and Z directions accordingly, and X_{cw}, Y_{cw}, and Z_{cw} are coordinate of points for a clockwise helix. R is the radius of the helix, φ is the winding angle, and θ is the helix angle (braid angle). The only difference between (A-1) and (A-2) is the π phase difference in Y coordinate which is shown by a negative sign in (A-2) ($\sin(\varphi + \pi) = -\sin(\varphi)$). A set of clockwise and counterclockwise helix paths with R = 15 mm, $0 < \varphi < 2\pi$, and $\theta = 30°$ are shown in A- Figure 1. A- Figure 1 a) shows the 3D model of

two helix paths – one clockwise (red) and one counterclockwise (blue), A- Figure 1b) shows the top view (X-Y) of the helix paths, which would be relevant to the cross-section view of the mandrel used for the TBC, and A- Figure 1 c) shows the right plane (X-Z) of the helix path where the helix angle is relevant to the braid angle.

a)   b)   c)
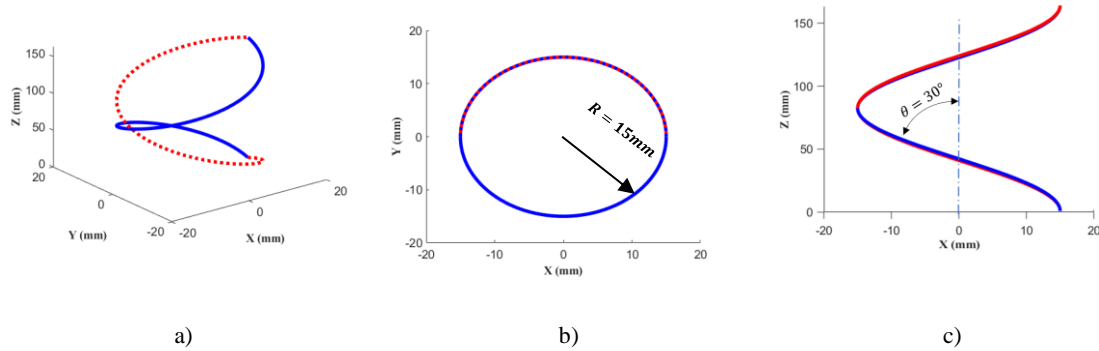
A- Figure 1 A counterclockwise (right-hand) (blue) and a clockwise (left-hand) (red) helix path with R = 15 mm and $\theta = 30°$ for one period ($0 < \varphi < 2\pi$). a) the 3D view, b) the top view, and c) right (x-z) view

On the other hand, each yarn path follows a sinusoidal path based on its braiding pattern. The equation relating the number of yarns, the radius of the strand, and the winding angle to the sinusoidal yarn path is shown in (A-3) [11].

$$S(\varphi) = r \sin\left(\frac{N\varphi}{2}\right) \tag{A-3}$$

Where r is the radius of the yarn and N is the total number of yarns. One of the undulation paths of a set of a sinusoidal path with $r = 0.7$ mm, $N = 4$, and $0 < \varphi < 2\pi$ is shown in A- Figure 2.
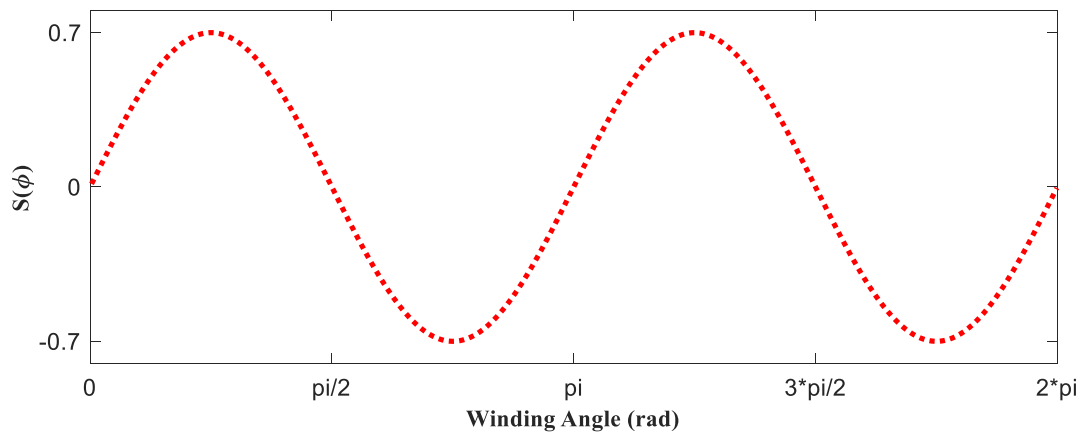
A- Figure 2 General sinusoidal paths of a yarn path with $r = 0.7\ mm$, $N = 4$, and $0 < \varphi \leq 2\pi$

For having the complete yarn path of braided composite, with helix shape and including the undulations, equations (A-1) and (A-2) should be mixed with equation (A-3). By doing so, equations (A-4) and (A-5) are created for counterclockwise and clockwise yarn paths, respectively.

$$
\begin{aligned}
X_i &= \big(R + S_1(\varphi)\big)\cos(\varphi + (i-1)\omega) & i &= 1,2 \dots n \\
Y_i &= \big(R + S_1(\varphi)\big)\sin(\varphi + (i-1)\omega) & i &= 1,2 \dots n \\
Z_i &= R\varphi \tan\theta & i &= 1,2 \dots n
\end{aligned}
\tag{A-4}
$$

$$
\begin{aligned}
X_i &= \big(R + S_2(\varphi)\big)\cos(\varphi + (i-1)\omega) & i &= 1,2 \dots n \\
Y_i &= -\big(R + S_2(\varphi)\big)\sin(\varphi + (i-1)\omega) & i &= 1,2 \dots n \\
Z_i &= R\varphi \tan\theta & i &= 1,2 \dots n
\end{aligned}
\tag{A-5}
$$

Where n is the number of the braiding yarns revolving in the same direction (i.e., $n = N/2$), i is the counter defining the actual braiding yarn revolving in the same direction, and ω is the shift angle which is calculated as the angle between every two strands (i.e., $\omega = 2\pi/n$). These equations are the same for all patterns of TBC. The only factor making the difference for each yarn pattern is $S_1(\varphi)$ and $S_2(\varphi)$ which will be discussed in the following sections.

Diamond pattern

The Diamond pattern is the most straightforward pattern of the TBC because the whole path is sinusoidal, and no flat section is incorporated into the path. The $S_1(\varphi)$ and $S_2(\varphi)$, representing the counterclockwise and clockwise sinusoidal paths respectively are as follows:

$$
S_1(\varphi) = r\sin\left(\frac{N\varphi}{2} + \frac{\pi}{2}\right)
\tag{A-6}
$$

$$
S_2(\varphi) = -r\sin\left(\frac{N\varphi}{2} + \frac{\pi}{2}\right)
\tag{A-7}
$$

A sample of the sinusoidal path of Diamond pattern with $r = 0.7\ mm$, $N = 2$, and $0 < \varphi \le 2\pi$ is shown in A- Figure 3.
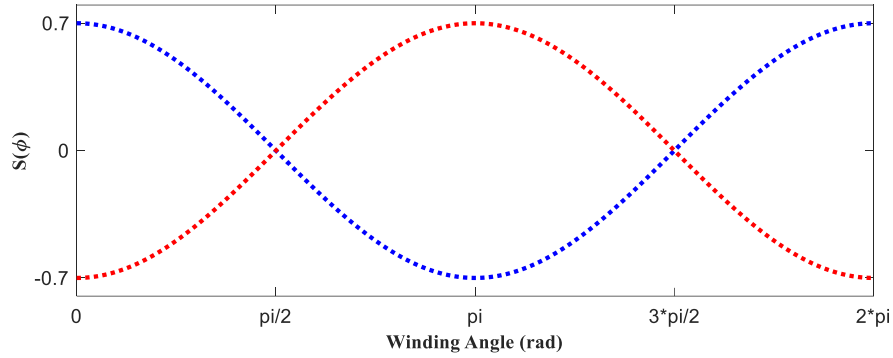
A- Figure 3 Counterclockwise (blue) and clockwise (red) undulation path of Diamond pattern

By adding equations (A-6) and (A-7) to (A-4) and (A-5), the equations for the 3-D path of the Diamond pattern will be generated. A sample of Diamond TBC yarn path (counterclockwise and clockwise) with $N = 32$, $R = 10$ mm, $r = 0.5$ mm, and $\theta = 45°$ is shown in A- Figure 4 (only one of the yarn at each direction is shown for more clarity). The radius of the mandrel is ($R_m = R - 2r$).
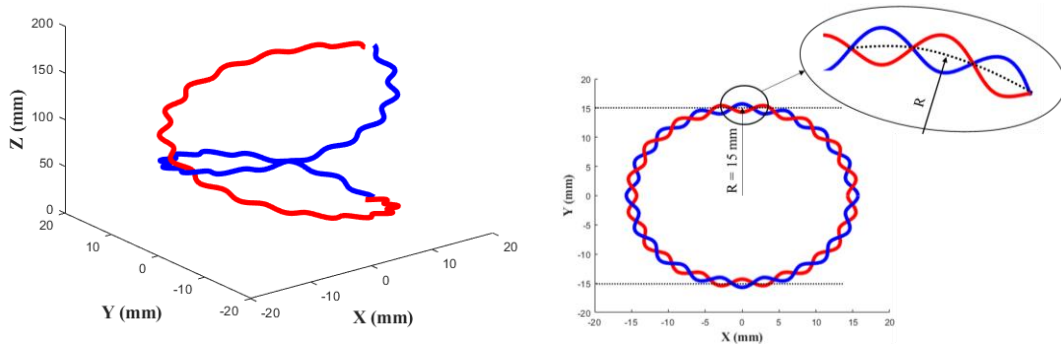
A- Figure 4 Clockwise (red) and counterclockwise (blue) yarn path of Diamond patterns with $N = 32$, $R = 15\ mm$, r=0.7 mm, and α=30° (only one set of yarns are shown)

Regular pattern

The shape of the Regular pattern is based on the Diamond pattern. Each yarn passes over two yarns moving in the other direction and under two others in the Regular pattern. Because of that, the Regular pattern involves a flat section for the distance between yarns. However, the transient area-going from the top of two yarns to the under the two next and vice versa- is still covered by the sinusoidal equations shown in the previous section. A sample of Regular undulation paths with $r = 0.7\ mm$, $N = 4$, and $0 < \varphi \leq 2\pi$ is shown in A- Figure 5.
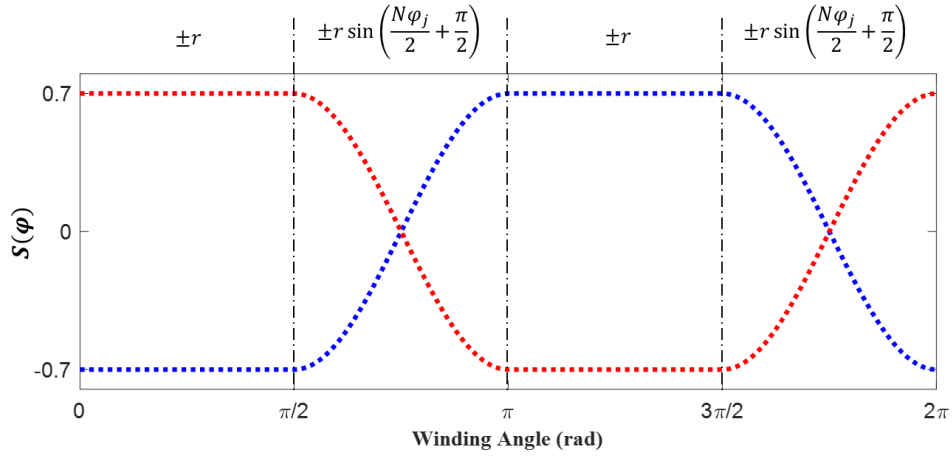
A- Figure 5 Counterclockwise (blue) and clockwise (red) undulation path of Regular pattern with $r = 0.7\ mm$, $N = 4$, and $0 < \varphi \leq 2\pi$

For generating the Regular yarn path, a set of piecewise equations as shown in equations (A-8) to (A-11) should be used. In addition, to make the ridges parallel to the axis of the TBC, two more piecewise equations, compared to the Diamond pattern, with π degree phase difference should be added. Therefore, there would be two sets of equations for counterclockwise undulation (A-8 and A-9) and two sets of equations for clockwise undulations (A-10 and A-11).

$$S_{1a}(\varphi_j) = \begin{vmatrix} r\sin\left(\dfrac{N\varphi_j}{2} + \dfrac{\pi}{2}\right) & ; 0 \leq \varphi_j < \theta/2 \\[2mm] -r & ; \theta/2 \leq \varphi_j < \theta \\[2mm] -r\sin\left(\dfrac{N\varphi_j}{2} + \dfrac{\pi}{2}\right) & ; \theta \leq \varphi_j < 3\theta/2 \\[2mm] r & ; 3\theta/2 \leq \varphi_j < 2\theta \end{vmatrix} \qquad \text{(A-8)}$$

$$S_{1b}(\varphi_j) = \begin{vmatrix} -r\sin\left(\dfrac{N\varphi_j}{2} + \dfrac{\pi}{2}\right) & ; 0 \leq \varphi_j < \theta/2 \\[2mm] r & ; \theta/2 \leq \varphi_j < \theta \\[2mm] r\sin\left(\dfrac{N\varphi_j}{2} + \dfrac{\pi}{2}\right) & ; \theta \leq \varphi_j < 3\theta/2 \\[2mm] -r & ; 3\theta/2 \leq \varphi_j < 2\theta \end{vmatrix} \qquad \text{(A-9)}$$

$$S_{2a}(\varphi_j) = \begin{vmatrix} -r & ; 0 \leq \varphi_j < \theta/2 \\[2mm] r\sin\left(\dfrac{N\varphi_j}{2} + \dfrac{\pi}{2}\right) & ; \theta/2 \leq \varphi_j < \theta \\[2mm] r & ; \theta \leq \varphi_j < 3\theta/2 \\[2mm] -r\sin\left(\dfrac{N\varphi_j}{2} + \dfrac{\pi}{2}\right) & ; 3\theta/2 \leq \varphi_j < 2\theta \end{vmatrix} \qquad \text{(A-10)}$$

$$S_{2b}(\varphi_j) = \begin{vmatrix} r & ; 0 \le \varphi_j < \theta/2 \\ -r\sin\left(\dfrac{N\varphi_j}{2} + \dfrac{\pi}{2}\right) & ; \theta/2 \le \varphi_j < \theta \\ -r & ; \theta \le \varphi_j < 3\theta/2 \\ r\sin\left(\dfrac{N\varphi_j}{2} + \dfrac{\pi}{2}\right) & ; 3\theta/2 \le \varphi_j < 2\theta \end{vmatrix} \qquad (A\text{-}11)$$

Where $j = 0,1,2,\ldots length(\varphi)$.

By combining equations (A-8) and (A-9) with equations (A-4) and equations (A-10) and (A-11) with equation (A-5), the yarn path of the Regular pattern will be achieved. Equations (A-4 and A-5 should be adopted based on the two new sets of equations as well). A sample of braid yarn with a Regular pattern, with $N = 32$, $\alpha = 60°$, $R = 11.4\ mm$, and $r = 0.7\ mm$ is shown in A- Figure 6 (only one of the yarn at each direction is shown for more clarity).
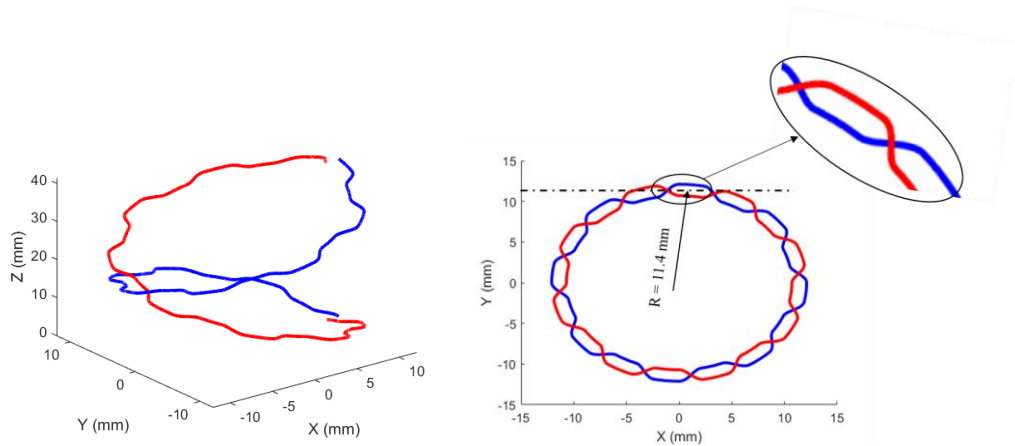
A- Figure 6 Clockwise (red) and counterclockwise (blue) yarn path of Regular pattern with $N = 32$, $R = 11.4\ mm$, $r = 0.7\ mm$, and $\theta = 60°$ (only one set of yarns are shown)

Hercules pattern

Hercules pattern is similar to Regular and Diamond patterns in terms of the sinusoidal and flat section. However, since in the Hercules pattern, a yarn passes above three yarns and then goes under the next three yarns, the flat section is two times longer than the Regular pattern. A sample of counterclockwise and clockwise undulation path of Hercules pattern with $r = 0.7\ mm$, $N = 8$, and $0 < \varphi \le 2\pi$ is shown in A- Figure 7.

As one can see, the flat sections are twice longer than the Regular pattern. The

sinusoidal undulations are the same as for Regular and Diamond patterns.
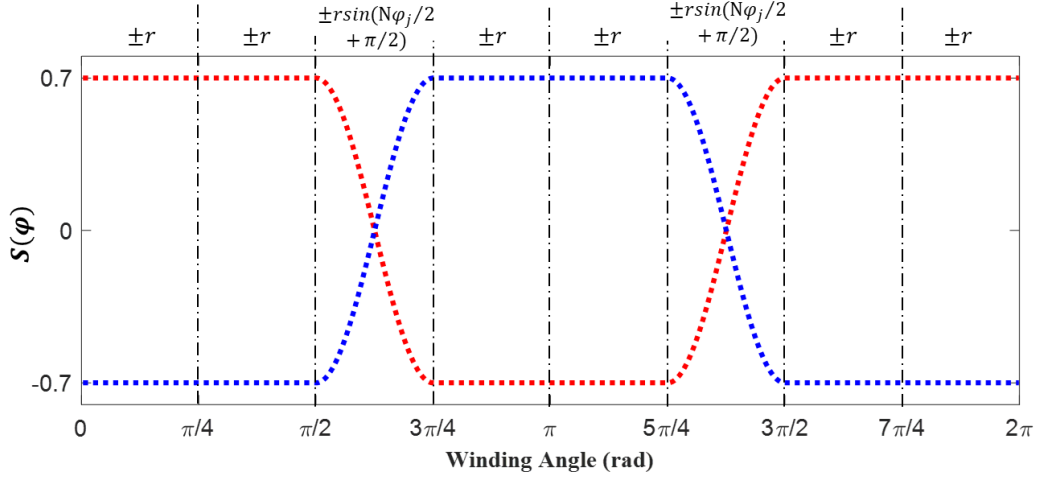
A- Figure 7 Counterclockwise (blue) and clockwise (red) undulation path of Hercules pattern with $r = 0.7\ mm$, $N = 8$, and $0 < \varphi \leq 4\pi$

The counterclockwise and clockwise equations for the Hercules pattern's undulation

path are shown in (A-12) and (A-13), respectively.

$$
S_1(\varphi_j) = \begin{vmatrix} r \\ r \\ r\sin\left(\dfrac{N\varphi_j}{2} + \dfrac{\pi}{2}\right) \\ -r \\ -r \\ r\sin\left(\dfrac{N\varphi_j}{2} + \dfrac{\pi}{2}\right) \end{vmatrix} \quad \begin{array}{l} ; 0 \leq \varphi_j < \omega/2 \\ ; \omega/2 \leq \varphi_j < \omega \\ ; \omega \leq \varphi_j < 3\omega/2 \\ ; 3\omega/2 \leq \varphi_j < 2\omega \\ ; 2\omega \leq \varphi_j < 5\omega/2 \\ ; 5\omega/2 \leq \varphi_j < 3\omega \end{array} \qquad \text{(A-12)}
$$

$$
S_2(\varphi_j) = \begin{vmatrix} -r \\ -r \\ -r\sin\left(\dfrac{N\varphi_j}{2} + \dfrac{\pi}{2}\right) \\ r \\ r \\ -r\sin\left(\dfrac{N\varphi_j}{2} + \dfrac{\pi}{2}\right) \end{vmatrix} \quad \begin{array}{l} ; 0 \leq \varphi_j < \omega/2 \\ ; \omega/2 \leq \varphi_j < \omega \\ ; \omega \leq \varphi_j < 3\omega/2 \\ ; 3\omega/2 \leq \varphi_j < 2\omega \\ ; 2\omega \leq \varphi_j < 5\omega/2 \\ ; 5\omega/2 \leq \varphi_j < 3\omega \end{array} \qquad \text{(A-13)}
$$

Similar to Diamond and Regular pattern equations, by combining equations (A-12) and

(A-13) by equations (A-4) and (A-5), the equations for the Hercules pattern will be

achieved. A sample of Hercules pattern with $N = 32$, $\gamma = 60°$, $R = 12\ mm$, and $r =$

0.7 *mm* is shown in A- Figure 8 (only one of the yarn at each direction is shown for more clarity).
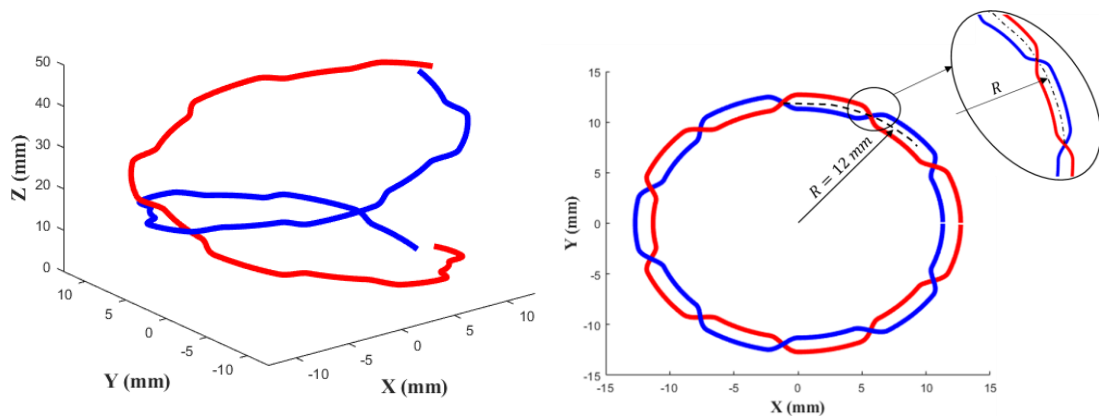
A- Figure 8 Clockwise (red) and counterclockwise (blue) yarn path of Hercules pattern with N=32, R=12 mm, r=0.7 mm, and γ=60° (only one set of yarns are shown)